

Controlled Synthesis, Characterization, and Catalytic Properties of Mn_2O_3 and Mn_3O_4 Nanoparticles Supported on Mesoporous Silica SBA-15

Yi-Fan Han,* Fengxi Chen, Ziyi Zhong, Kanaparthi Ramesh, Luwei Chen, and Effendi Widjaja

Institute of Chemical and Engineering Sciences, 1, Pesek Road, Jurong Island, Singapore 627833

Received: August 2, 2006; In Final Form: August 29, 2006

A method established in the present study has proven to be effective in the synthesis of Mn_2O_3 nanocrystals by the thermolysis of manganese(III) acetyl acetonate ($[\text{CH}_3\text{COCH}=\text{C}(\text{O})\text{CH}_3]_3\text{Mn}$) and Mn_3O_4 nanocrystals by the thermolysis of manganese(II) acetyl acetonate ($[\text{CH}_3\text{COCH}=\text{C}(\text{O})-\text{CH}_3]_2\text{Mn}$) on a mesoporous silica, SBA-15. In particular, Mn_2O_3 nanocrystals are the first to be reported to be synthesized on SBA-15. The structure, texture, and electronic properties of nanocomposites were studied using various characterization techniques such as N_2 physisorption, X-ray diffraction (XRD), laser Raman spectroscopy (LRS), temperature-programmed reduction (TPR), transmission electron microscopy (TEM), and X-ray photoelectron spectroscopy (XPS). The results of powder XRD at low angles show that the framework of SBA-15 remains unaffected after generation of the manganese oxide (MnO_x) nanoparticles, whereas the pore volume and the surface area of SBA-15 dramatically decreased as indicated by N_2 adsorption–desorption. TEM images reveal that the pores of SBA-15 are progressively blocked with MnO_x nanoparticles. The formation of the hausmannite Mn_3O_4 and bixbyite Mn_2O_3 structures was clearly confirmed by XRD. The surface structures of MnO_x were also determined by LRS, XPS, and TPR. The crystalline phases of MnO_x were identified by LRS with corresponding out-of-plane bending and symmetric stretching vibrations of bridging oxygen species ($\text{M}-\text{O}-\text{M}$) of both MnO_x nanoparticles and bulk MnO_x . We also observed the terminal $\text{Mn}=\text{O}$ bonds corresponding to vibrations at 940 and 974 cm^{-1} for $\text{Mn}_3\text{O}_4/\text{SBA-15}$ and $\text{Mn}_2\text{O}_3/\text{SBA-15}$, respectively. These results show that the MnO_x species to be highly dispersed inside the channels of SBA-15. The nanostructure of the particles was further identified by the TPR profiles. Furthermore, the chemical states of the surface manganese (Mn) determined by XPS agreed well with the findings of LRS and XRD. These results suggest that the method developed in the present study resulted in the production of MnO_x nanoparticles on mesoporous silica SBA-15 by controlling the crystalline phases precisely. The thus-prepared nanocomposites of MnO_x showed significant catalytic activity toward CO oxidation below 523 K. In particular, the MnO_x prepared from manganese acetyl acetonate showed a higher catalytic reactivity than that prepared from $\text{Mn}(\text{NO}_3)_2$.

Introduction

Manganese oxides (MnO_x) are of great importance in catalysis, electrochemistry, ion-exchange materials, magnetite, and batteries, among other areas.^{1–4} In the recent past, controlled synthesis of MnO_x nanomaterials has attracted considerable attention from both academia and industry.^{5–7} Among various preparation methods using porous materials as solid nanoreactors, MnO_x nanocrystals with various morphologies, e.g., nanoarrays, nanowires, nanospheres, and clusters, have been obtained by a method called “nanocasting”.^{8,9} Generally, inorganic precursors are first introduced into channels of host materials, such as mesoporous silicas. Then, MnO_x nanocrystals are produced with a replica of the confined space by a subsequent calcination. Because of the facile phase transformation of MnO_x during preparation, only multivalence mixtures of manganese oxides (MnO_2 , Mn_2O_3 , and Mn_3O_4) are usually obtained. To date, direct synthesis of manganese oxide with a defined crystalline structure in nanoreactors, especially silica-based materials, is still far from easy. Mn_2O_3 nanoparticles can be produced through a conventional method, namely, thermal

treatment of MnO_2 above 823 K or reduction in H_2 above 523 K.^{10–13} Actually, both high-temperature treatment and H_2 reduction can usually give rise to the aggregation and phase transformation of MnO_x nanoparticles. Although the generation of Mn_3O_4 nanoparticles from Mn-containing organic clusters¹² and the synthesis of MnO_2 nanoparticles from $\text{Mn}(\text{NO}_3)_2$ ¹³ inside SBA-15 have been reported recently, the fabrication of Mn_2O_3 nanoparticles on mesoporous materials has rarely been addressed so far.

Presently, there is a growing interest in precisely controlling the crystalline phase of manganese oxide at the nanoscale in order to understand the mechanistic aspects of CO oxidation at low temperatures. Furthermore, MnO exhibits unique antiferromagnetic character at temperatures below $T_N = 118$ K, and it becomes an ideal material for the study of electronic and magnetic properties of rock salt oxides;¹⁴ MnO_2 and Mn_3O_4 are widely used as catalysts and electrode materials.¹⁵ In addition, we recently observed that bulk Mn_2O_3 could potentially be a highly efficient combustion catalyst at low temperatures (<527 K) for pollution control.¹⁶

Synthesis of supported metal oxides with high dispersion is of great importance. The structure and dispersion depend primarily on the preparation method, the nature of the support,

* To whom correspondence should be addressed. E-mail: han_yi_fan@ices.a-star.edu.sg.

and the type of precursor itself. Ordered mesoporous materials with their intrinsically high surface areas are particularly suitable for this purpose. There is a growing interest in replacing traditional precursors such as chlorides and nitrates in the synthesis of supported metals and metal oxides with metal acetyl acetonates in either the presence or absence of oxygen.¹² The reasons for such a uniform dispersion is the formation of nanoparticles because their bulky acetyl acetonate ligands are able to isolate the central metal ion. Generally, metal acetyl acetonates are treated at high temperatures in the presence of oxygen to form corresponding oxides. It is well-known that SBA-15 is one of the most attractive host materials, because of its unique mesostructure features, such as large uniform pore size (5–30 nm), high surface area (600–1000 m²/g), thicker silica walls (3.1–6.4 nm), and high thermal stability (up to ~1000 K).^{17,18} More recent studies have demonstrated that SBA-15 can be a promising template for the synthesis of metal oxide nanocrystals.^{8,9,19}

On the other hand, a literature survey reveals that the catalytic performance of MnO_x nanoparticles as oxidation catalysts has not been fully recognized. In particular, little attention has been paid to the catalytic behavior of the MnO_x catalysts in oxidation/combustion reactions at low temperatures, e.g., below ca. 573 K, which are usually performed with noble metal catalysts. Generally, catalytic activities over transition metal oxide catalysts are lower than those over noble metal catalysts. However, the inherent advantages of metal oxide catalysts, such as low cost, high thermal stability, and high mechanical strength, make them a promising alternative in several catalytic applications.

In this context, the present study considers the controlled synthesis of MnO_x on SBA-15 support by a molecularly designed dispersion method. The present investigation is also directed toward a better understanding of the catalyst structure, dispersity, and catalytic properties of the MnO_x nanoparticles on the mesoporous silica SBA-15. Significant activity of various MnO_x nanoparticles has been reported in oxidation/combustion reactions applied for pollution control.^{20,21} In this work, we examined the tremendous reactivity of the as-prepared MnO_x nanoparticles during CO oxidation for the first time, which is an emerging process driven primarily by environmental and energetic concerns.^{22–24} A preliminary effort to identify a correlation between the surface properties of MnO_x nanoparticles and their catalytic activity has been undertaken.

Experimental Section

1. Preparation. Synthesis of SBA-15. Synthesis of SBA-15 was conducted according to a reported method with modifications.¹⁸ Pluronic P123 (BASF) was used as a template, and the silica source was tetraethyl orthosilicate (TEOS, 98%), which was added dropwise to an acidic P123 aqueous solution and then stirred at 313 K for 24 h at 600 rpm. The pH value of the reaction mixture was adjusted by adding HCl (37%) aqueous solution. The molar ratio of the reaction mixture was TEOS/P123/HCl/H₂O = 1/0.0168/5.8/155. The resulting mixture was aged at 338 K for 5 days. The powder was recovered by filtration and dried at 383 K overnight. It was further calcined at 823 K for 5 h in static air at a ramping rate of 1 K/min.

Synthesis of MnO_x Nanoparticles. Manganese(II) acetyl acetonate (acac) ([CH₃COCH=C(O)–CH₃]₂Mn, Aldrich) and manganese(III) acetyl acetonate ([CH₃COCH=C(O)–CH₃]₃Mn, Aldrich) in a ratio of 2.5 mmol/g of SBA-15 were dissolved in acetone (C.P.) at room temperature. The SBA-15 powder was then placed into the solution after the manganese acetyl

acetonates had completely dissolved. The precursors were obtained by vigorously stirring the solutions until the solvent had evaporated completely and then washed with acetone several times to remove residues remaining on the SBA-15 surface. Finally, the precursors were calcined in an oven (exposed to static air) at 773 K for 5 h at a ramping rate of 1 K/min. Through calcination, the organic compounds transformed directly into Mn₃O₄ and Mn₂O₃ nanocrystals. Note that thermal decomposition of mixtures of manganese(II) and manganese(III) acetyl acetonates under the same calcination conditions produced only mixed MnO_x (mainly MnO₂, dark color). For the purpose of comparing reactivities, MnO_x/SBA-15 sample (2.5 mmol of Mn/g of SBA-15) was prepared by impregnating an aqueous Mn(NO₃)₂ solution (Aldrich) and treated in the same way. The loading amount of MnO_x with respect to SBA-15, confirmed by the ICP analysis, was ca. 13 wt %.

2. Characterization. X-ray Diffraction (XRD). Powder X-ray diffraction data were obtained with a Bruker D8 diffractometer using Cu Kα radiation ($\lambda = 1.540589$ Å). The diffraction patterns were recorded in the Bragg angle (2θ) ranges of 0.6–5° and 30–60° at room temperature. Note that the high-angle powder XRD (PXRD) patterns were obtained by scanning overnight (XRD, step size of 0.02° per step, 8 s per step, 14 h for scanning 30°).

Transmission Electron Microscopy (TEM). All samples were ultrasonically dispersed in ethanol solvent and then dried over a carbon grid. The measurements were performed on a Tecnai TF 20 S-twin instrument with a Lorentz lens. For the images shown here, only silica grains along the [001] orientation were selected.

Laser Raman Spectroscopy (LRS). The dispersive Raman microscope employed in this study was a JY Horiba LabRAM HR instrument equipped with three laser sources (ultraviolet, visible, and near-infrared), a confocal microscope, and a liquid-nitrogen-cooled charge-coupled device (CCD) multichannel detector (256 pixels × 1024 pixels). The visible 514.5-nm argon ion laser was selected to excite the Raman scattering. The laser power from the source was around 20 mW, but when it reached the samples, the laser output was reduced to around 6–7 mW after passing through filtering optics and a microscope objective. A 100× objective lens was used, and the acquisition time for each Raman spectrum was approximately 60–120 s depending on the sample. The Raman shifts acquired were in the range of 200–1000 cm^{−1} with a spectral resolution 1.7–2 cm^{−1}.

X-ray Photoelectron Spectroscopy (XPS). XPS analysis was performed on a VG ESCALAB 250 spectrometer, using Al Kα radiation (1486.6 eV, pass energy of 20.0 eV). The base pressure of the instrument is 1×10^{-9} Torr. The background contribution B (E) (obtained by the Shirley method) caused by inelastic processes was subtracted, and curve fitting was performed with a Gaussian–Lorentzian profile using standard software. The binding energies (BEs) over supported catalysts were calibrated using the Si 2p peak at 103.1 eV and the C 1s peak at 85.0 eV. The instrument was also calibrated using Au wire. XPS spectra were recorded at $\theta = 90^\circ$ for the X-ray sources. The atom ratios of oxygen to manganese (O/Mn) were calculated using the equation^{25,26}

$$\frac{N_{\text{O}}}{N_{\text{Mn}}} = \frac{I_{\text{O}}/S_{\text{O}}}{I_{\text{Mn}}/S_{\text{Mn}}}$$

where I_{Mn} and I_{O} are the time-normalized intensities of the Mn 2p and O 1s levels, respectively, and S_{O} (0.711 for O 1s) and S_{Mn} (2.420 for Mn 2p) are the corresponding atomic sensitivity

factors for X-ray sources at 90°. The BEs for O 1s at 529.0–530.0 eV are attributed to the contributions from manganese oxides.²⁷

N₂ Adsorption–Desorption. N₂ adsorption and desorption isotherms were collected on an Autosorb-6 instrument at 77 K. Prior to the measurements, all samples were degassed at 573 K until a stable vacuum of ca. 5 mTorr was reached. The pore size distribution curves were calculated from the adsorption branch using the Barrett–Joyner–Halenda (BJH) method. The specific surface area was assessed using the BET method from adsorption data in a relative pressure range from 0.06 to 0.10. The total pore volume, *V_t*, was assessed from the adsorbed amount at a relative pressure of 0.99 by converting it to the corresponding volume of liquid adsorbate. The conversion factor between the volume of gas and liquid adsorbate is 0.0015468 for N₂ at 77 K when the values are expressed in cm³/g and cm³ STP/g, respectively.

Temperature-Programmed Reduction (TPR). Prior to the experiments, all samples (50 mg) were purged with Ar at 523 K at a flow rate of 20 mL/min for 2 h so that most of the physically adsorbed H₂O could be removed from the catalysts. The TPR was performed in a micro-fixed-bed reactor connected to a GC-QMS (HPR-20, Hidden Analytical Ltd.), where various mass-to-charge ratios of *m/e* = 2, 16, 18, and 28 were monitored. The temperature was ramped from 323 to 1100 K at a linear heating rate of 10 K/min in a carrier gas of H₂ (5.0 kPa + Ar) for TPR at a flow rate of 50 mL/min.

3. Reactivity Measurements. Activity measurements were carried out in a micro-plug-flow reactor. Before each experiment, the dried catalyst was conditioned in situ by being heated in Ar at 523 K (2 h, 30 mL/min). The reaction was measured in a stream of 5.0 kPa CO, 5.0 kPa O₂, and the balance Ar at a space velocity of 6000 h^{−1}. The reactivity of the catalysts was very stable: loss of ca. 10% of the reactivity was observed at 473 K after a time-on-stream of 10 h. The analysis of the reactant was done with an online GC (Shimadzu GC-14B) equipped with a carbosieve-II column.

As a reference, high-purity bulk manganese oxides (MnO_x) MnO (Aldrich, 99.99%, 1.1 m²/g), Mn₃O₄ (Aldrich, 97.0%, 1.1 m²/g), α-Mn₂O₃ (Aldrich, 99.999%, 4.0 m²/g), and β-MnO₂ (Aldrich, 99.999%, 0.9 m²/g), as received, were also tested for CO oxidation and characterized by the XPS and LRS techniques. Scanning electron microscopy (SEM, JEOL, JBM-6700F) revealed that the particle size for all bulk MnO_x samples (commercial) was randomly distributed in the range of 0.06–0.7 μm, corresponding to an average particles size of ~0.5 μm. Note that the granule size of the SBA-15 powder is estimated to be ca. 325 μm. The effects of external diffusion during reaction can be safely ruled out.

3. Results and Discussion

PXRD and N₂ Adsorption. The crystalline phases of MnO_x nanoparticles and the SBA-15 features were determined by PXRD. The low-angle PXRD patterns of SBA-15 and MnO_x/SBA-15 are shown in Figure 1. The low-angle XRD pattern of the SBA-15 (Figure 1A) sample showed three distinct Bragg diffraction peaks, (100), (110), and (200), which indicate the formation of a highly ordered two-dimensional hexagonal mesoscopic structure. Figure 1B,C suggests that SBA-15 still has a high degree of hexagonal mesoscopic organization even after insertion of MnO_x nanocrystals.¹⁸ It was seen that, upon calcination of Mn(acac)₂- or Mn(acac)₃-loaded SBA-15 precursors at 773 K for 5 h in air, their low-angle XRD peaks shifted toward higher angles (Figure 1), because the unit cell parameter

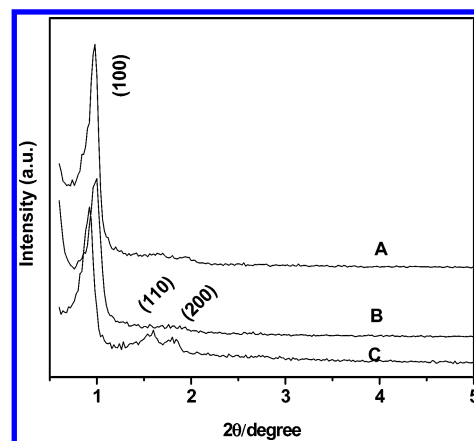


Figure 1. Powder XRD patterns of manganese oxide nanocrystals on SBA-15 at low angles: (A) Mn₃O₄/SBA-15, (B) Mn₂O₃/SBA-15, and (C) SBA-15.

TABLE 1: Textural Properties of SBA-15 and MnO_x/SBA-15

sample	<i>a</i> ₀ (Å) ^a	<i>S</i> _{BET} (m ² /g)	<i>V_p</i> (cm ³ /g)	<i>D_p</i> (Å)
SBA-15	111.8	937	1.27	77.2
Mn ₃ O ₄ /SBA-15	104.4	299	0.49	63.4
Mn ₂ O ₃ /SBA-15	102.4	226	0.38	56.2

^a The unit cell parameter, *a*₀, was calculated from the (100) reflection according to the formula *a*₀ = 2*d*₁₀₀/√3.

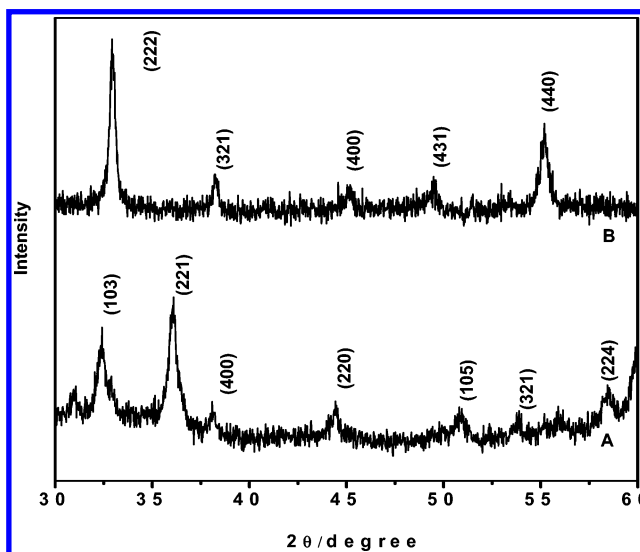


Figure 2. Powder XRD patterns of manganese oxide nanocrystals on SBA-15 at high angles: (A) Mn₃O₄/SBA-15, (B) Mn₂O₃/SBA-15.

of SBA-15 became smaller (Table 1). The observed unit cell contraction of SBA-15 (ca. 6–8%) should be due to the further condensation of silica framework of SBA-15 during calcination of manganese complexes. Several peaks at high angles in the XRD pattern, as shown in Figure 2A,B, indicate the formation of well-crystallized hausmannite Mn₃O₄ (JCPDS 80-0382) and bixbyite α-Mn₂O₃ (JCPDS 41-1442), respectively. N₂ adsorption and desorption isotherms were measured on all samples to evaluate the surface and structural properties. The N₂ adsorption curves are presented in Figure 3, and the data are summarized in Table 1. Both pure SBA-15 and MnO_x/SBA-15 samples exhibited adsorption isotherms of type IV with hysteresis loops, which are characteristic of nanostructured materials with uniform mesopores. The adsorption and desorption isotherms showed a large increase in the relative pressure (*P/P*₀) ranging from 0.6 to 0.8 for SBA-15 and from 0.5 to 0.7 for MnO_x on SBA-

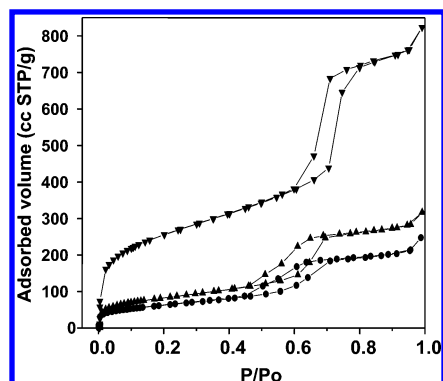


Figure 3. N₂ adsorption–desorption isotherms: (▼) SBA-15, (▲) Mn₃O₄/SBA-15, (●) Mn₂O₃/SBA-15.

15, which is caused by capillary condensation into the mesopores. The N₂ adsorption data presented in Table 1 show that the pore volume decreased markedly from 1.27 cm³/g for SBA-15 to 0.49 cm³/g for Mn₃O₄/SBA-15 and 0.38 cm³/g for Mn₂O₃/SBA-15, whereas the average pore diameter of SBA-15 was about 7.7 nm and decreased slightly to 6.3 nm for Mn₃O₄/SBA-15 and 5.6 nm for Mn₂O₃/SBA-15. The decrease in pore volume can be attributed to the formation of MnO_x nanoparticles. The specific surface area of SBA-15 was found to be 937 m²/g and decreased rapidly to 299 and 266 m²/g for Mn₃O₄ and Mn₂O₃, respectively, supported on SBA-15, indicating that the pores were progressively blocked by MnO_x nanoparticles.

TEM. The morphology and structure of the nanocomposites were further characterized with TEM. Obviously, the SBA-15 employed has the typical *p6mm* hexagonal morphology with well-ordered 1D arrays (see Figure 4a–c). The average pore size of SBA-15 (Figure 4a) is ca. 8 nm, which is very close to the value (ca. 7.7 nm) determined by N₂ adsorption. From the transverse sections of SBA-15 silica grains (along the [001] orientation), we can see the filled, partially filled, and empty pores. Figure 4b shows a typical feature of Mn₃O₄/SBA-15 that pore A is empty and has a hexagonal feature with a diameter of ca. 8.0 nm, pores B (diameter of 5.0 nm) and C (diameter of 2.5 nm) are partially filled with Mn₃O₄ nanoparticles, and pore D is completely filled. Similar features were also observed for Mn₂O₃/SBA-15, as shown in Figure 4c, where pore A is unfilled and pores B and C are occupied by Mn₂O₃.

The average size of both nanocrystals is about 15 nm based on the XRD patterns, according to the Scherrer formula. This value reflects the crystallite dimension normal to the reflecting plane. The two strongest reflections were used to calculate the average crystallite size in the present work; that is, the (103) and (221) peaks were used for Mn₃O₄/SBA-15, and the (222) and (440) peaks were used for Mn₂O₃/SBA-15. Therefore, the estimated sizes based on XRD patterns represent the average growth along the (103) and (221) directions for Mn₃O₄ and along the (222) and (440) directions for Mn₂O₃. The MnO_x nanoparticles in the present study were synthesized by using the cylindrical mesopores of SBA-15 as hard templates. As such, the morphology of the MnO_x particles is expected to be rodlike, and their radial growth is constrained by the pore diameter of SBA-15, which should be less than 7.0 nm. The TEM images shown in Figure 4 recorded along the [001] direction depict this scenario. On the other hand, the axial growth of the MnO_x particles along the cylindrical mesopores of SBA-15 is controlled by diffusion limitations and particle fusion. Therefore, their axial size can grow larger along the cylindrical mesopores, e.g., 15 nm estimated from XRD patterns. Such a greater particle size was also observed in TEM images of MnO_x/SBA-15

recorded along the [100] direction. Nevertheless, evaluation of the size of the MnO_x nanoparticles by TEM is still ongoing.

LRS. The crystalline phases and Mn valences of the MnO_x nanoparticles were further determined using LRS and XPS with reference to spectra acquired from bulk MnO_x. LRS data obtained for Mn₃O₄/SBA-15 and Mn₂O₃/SBA-15 under ambient conditions are shown in Figure 5A,C; LRS data for bulk Mn₃O₄ and Mn₂O₃ were also recorded simultaneously and are shown in Figure 5B,D. The bands at 309/310, 365, 502/472, and 641/651 cm⁻¹ detected for bulk MnO_x might correspond to the out-of-plane bending modes of Mn₂O₃/Mn₃O₄, the asymmetric stretch of bridge oxygen species (Mn–O–Mn), and the symmetric stretch of Mn₂O₃/Mn₃O₄ groups, respectively.^{28–31} Upon close examination of these spectra, we can find that the Raman bands were broadened and down-shifted when the particles became smaller. For instance, the distinct features at 641 cm⁻¹ for bulk Mn₂O₃ and 655 cm⁻¹ for the Mn₃O₄ shifted to 628 and 648 cm⁻¹, respectively, accompanied by broadening of the bands. Analogous results reported previously have been attributed to the effect of phonon confinements. Zuo et al. has already provided a detailed explanation for this phenomenon.^{32,33}

Interestingly, the bands appearing at 974 cm⁻¹ for Mn₂O₃/SBA-15 and 940 cm⁻¹ for Mn₃O₄/SBA-15, to our knowledge of Raman spectra of MnO_x-containing materials, have rarely been addressed previously. In a comparative survey of the mesoporous materials MCM-48 and Ti-MCM-48, Morey et al.³⁴ suggested that the Raman vibrations within the range of 960–980 cm⁻¹ might indicate the presence of silanol groups (Si–OH) inside the mesoporous channels (ca. 980 cm⁻¹) and Ti incorporation into the framework (ca. 965 cm⁻¹), which was a silica-based porous matrix related with the Si–OH defects. However, Figure 5E, acquired from pure SBA-15, does not show any peak in the range of 800–1000 cm⁻¹, which means that Si–OH defects are rare in the as-prepared SBA-15. Therefore, we can safely exclude the possible incorporation of Mn into the SBA-15 framework.

In principle, for transition metal oxides, the Raman bands in the wavenumber range of 800–1000 cm⁻¹ are usually assigned to the symmetric/asymmetric stretch of terminal metal oxide groups (M_xO_y).³⁰ Chua et al.²⁸ has pointed out that visible Raman is very sensitive to terminal oxygen vibrations (M=O) in metal oxides. For instance, the band at ~930 cm⁻¹ was assigned to Cr=O, representing the symmetric stretch of a terminal CrO₂ group or the asymmetric stretch of a terminal CrO₃ group for a 0.5% CrO₃/Al₂O₃ mixture; correspondingly, the band at ~950 cm⁻¹ for V=O appeared for a 20% V₂O₅/Al₂O₃ mixture and the band at ~945 cm⁻¹ for Mo=O appeared for a 18% MoO₃/Al₂O₃ mixture.²⁸ The bands at 974/940 cm⁻¹ might be associated with the stretch of a terminal Mn=O group, an indication of the existence of numerous isolated Mn₂O₃ and Mn₃O₄ groups.³⁰ It should be emphasized that these peaks did not appear for a MnO_x/SBA-15 mixture, for which the manganese oxides, mainly consisting of MnO₂, were prepared through calcination of impregnated Mn(NO₃)₂ in air. This fact indicates that the Mn source is a key factor in the fabrication of phase-defined MnO_x nanocrystals. We propose that the manganese acetyl acetonates can effectively be grafted to the inner wall of SBA-15 and isolated from each other, probably through the interaction of the organic compounds and the hydroxyl (–OH) group linked to the framework wall. Therefore, it is understandable that isolated or low polymeric MnO_x species might be anchored on the pore wall or the surface of SBA-15 silica. In particular, the strong intensity of the peak at 974 cm⁻¹, as shown in Figure

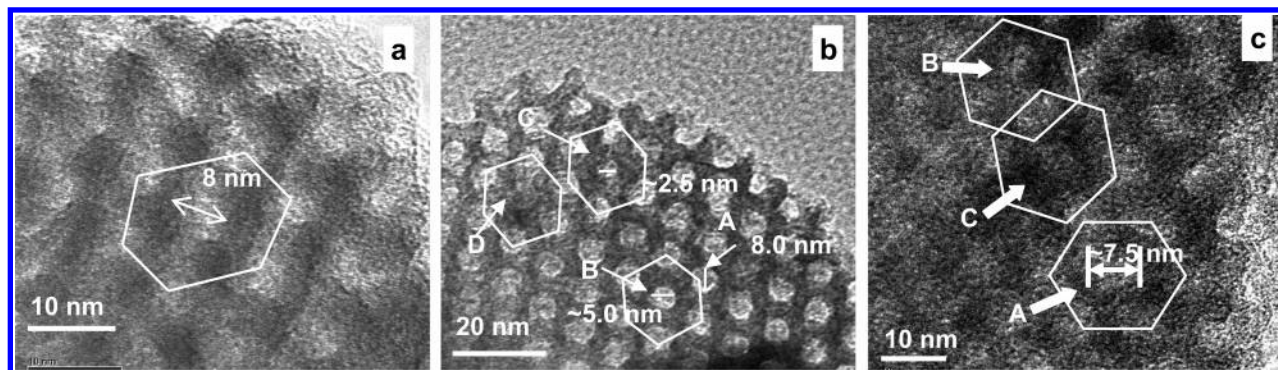


Figure 4. TEM images recorded along the [001] orientation of (a) SBA-15; (b) $\text{Mn}_3\text{O}_4/\text{SBA-15}$ with pore A unfilled with a hexagonal structure, pores B and C partially filled, and pore D completely filled; and (c) $\text{Mn}_2\text{O}_3/\text{SBA-15}$ with pore A unfilled, pore B partially filled, and pore C completely filled.

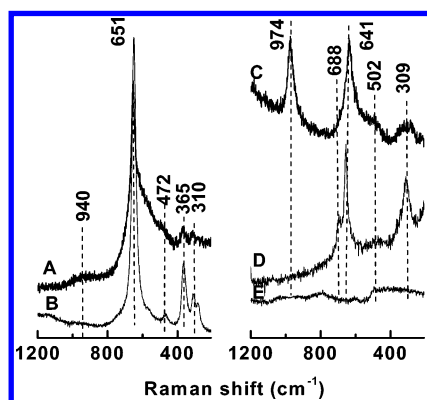


Figure 5. Raman spectroscopy of (A) $\text{Mn}_3\text{O}_4/\text{SBA-15}$, (B) pure bulk Mn_3O_4 , (C) $\text{Mn}_2\text{O}_3/\text{SBA-15}$, (D) pure bulk Mn_2O_3 , and (E) blank SBA-15.

5C, indicates that the dispersion of the MnO_x species using $\text{Mn}^{\text{III}}(\text{acac})_3$ is much higher than that of using $\text{Mn}^{\text{II}}(\text{acac})_2$.

XPS. On the other hand, additional information on Mn chemical states can be obtained from the XPS analysis. Currently, a great number of studies have been performed to detect the Mn–O system using XPS.^{35–39} Unfortunately, the variation of XPS binding energies of Mn 2p alone, from Mn^{2+} to Mn^{4+} , usually is too small (less than ca. 1.0 eV) to precisely evaluate the Mn valence of MnO_x . The assignment can be complicated further if the Mn present is in several chemical states. Therefore, the analysis of XPS results from MnO_x nanoparticles was carried out usually by comparison to spectra obtained from bulk MnO_x . In addition, the extent of Mn 3s multiplet splitting measured simultaneously (Mn 3s ΔE) offers additional insight into the Mn chemical states.

Mn 2p XPS spectra measured from bulk and supported MnO_x are shown in Figures 6 and 7, respectively. For the former, an increase of the Mn 2p BE, ca. 0.9 eV, with increasing Mn valence from 2+ to 4+ can be clearly seen in Figure 6, whereas the value of Mn 3s ΔE decreased from 6.3 to 4.5 eV as listed in Table 2. These results are analogous to those of previous XPS studies for the same materials.^{37–40} The Mn 2p XPS spectra shown in Figure 7 indicate that the Mn 2p BEs for nanoparticles are higher than those for the bulk by ca. 0.6–0.8 eV. The upward shift of the Mn 2p BEs for the MnO_x nanoparticles might result from the high dispersion of the Mn(III) ions on the SBA-15 surface, which leads to a stronger electrostatic field. Similarly, Kapteijn et al.⁴⁰ observed that the Mn 2p BEs acquired from a 2 wt % $\text{MnO}_x/\text{Al}_2\text{O}_3$ catalyst, assuming that Mn^{3+} was the predominant species, was about 1.0–1.5 eV higher than that from the bulk. However, the BE shifted to low values with increasing loading amount of MnO_x , because of the formation

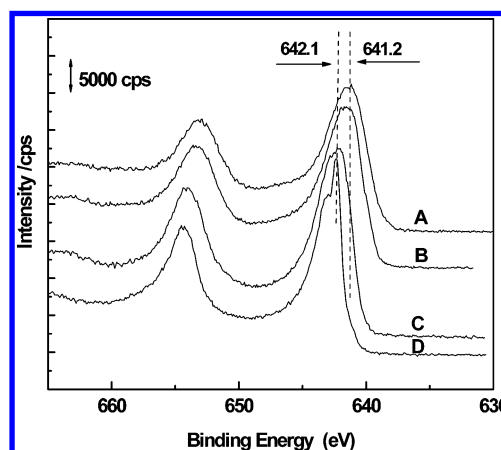


Figure 6. XPS Mn 2p spectra of pure bulk MnO_x : (A) MnO, (B) Mn_3O_4 , (C) $\alpha\text{-Mn}_2\text{O}_3$, (D) $\beta\text{-Mn}_2\text{O}_2$.

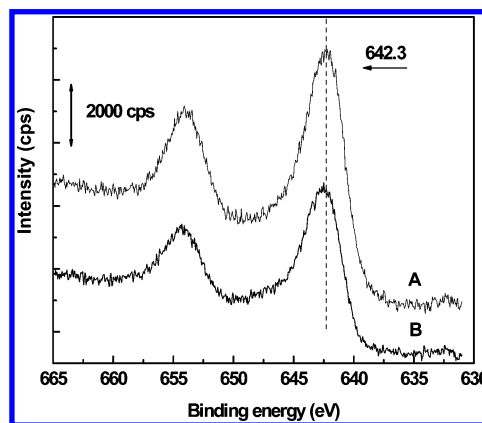


Figure 7. XPS Mn 2p spectra of fresh MnO_x nanocrystals: (A) $\text{Mn}_3\text{O}_4/\text{SBA-15}$, (B) $\text{Mn}_2\text{O}_3/\text{SBA-15}$.

of adlayers of Mn_2O_3 . Nevertheless, through the Mn 3s ΔE value obtained from both nanoscale and bulk MnO_x , the Mn valence can still be estimated, at least qualitatively, in agreement with the results from LRS. Moreover, additional information can also be obtained by comparing the XPS peak features. Table 2 shows that the full widths at half-maximum of the Mn 2p peak (FWHM) taken from the nanoparticles are obviously higher than those from the counterpart bulk MnO_x . For instance, the FWHM of ca. 3.3 eV for Mn 2p_{3/2} in bulk Mn_3O_4 increases to ca. 3.7 eV for $\text{Mn}_3\text{O}_4/\text{SBA-15}$. This might occur for two reasons: (i) the interaction between MnO_x and SBA-15 and (ii) a change in electronic properties with decreasing particle size. The O/Mn atomic ratios measured by XPS are very similar for both bulk MnO_x and MnO_x nanoparticles, as also listed in Table 2. This

TABLE 2: XPS Data for the Bulk and Nanocrystals MnO_x

sample	BE Mn 2p _{3/2} (fwhm) (eV)	BE Mn 2p _{1/2} (fwhm) (eV)	Mn 3s ΔE (eV)	O/Mn atomic ratio
MnO ^a	641.2 (3.3)	653.0 (3.3)	6.3	0.95
MnO ^b	641.2 (3.3)	653.1 (3.2)	6.4	0.97
Mn ₃ O ₄ ^a	641.7 (3.2)	653.4 (3.2)	4.6	1.29
Mn ₃ O ₄ ^b	641.8 (3.3)	653.6 (3.2)	4.6	1.30
Mn ₂ O ₃ ^a	641.8 (3.0)	654.1 (3.2)	4.9	1.67
Mn ₂ O ₃ ^b	641.8 (3.0)	654.2 (3.1)	5.0	1.65
MnO ₂ ^a	642.1 (2.2)	654.5 (2.7)	4.5	1.93
MnO ₂ ^b	642.3 (2.3)	654.5 (2.6)	4.5	2.0
Mn ₃ O ₄ /SBA-15 ^a	642.3 (3.7)	654.1 (3.5)	4.7	1.37
Mn ₃ O ₄ /SBA-15 ^b	642.3 (3.6)	654.3 (3.6)	4.6	1.40
Mn ₂ O ₃ /SBA-15 ^a	642.6 (3.5)	654.5 (3.4)	5.0	1.65
Mn ₂ O ₃ /SBA-15 ^b	642.7 (3.6)	654.6 (3.7)	5.1	1.63

^a Fresh catalysts were dehydrated at 473 K for 2 h in an Ar flow of 20 mL/min prior to XPS measurements. ^b Spent catalysts were from CO oxidation at 473 K for 10 h in a mixture of CO (5.0 kPa), O₂ (5.0 kPa), and Ar (balance) at a space velocity: 6000 h⁻¹.

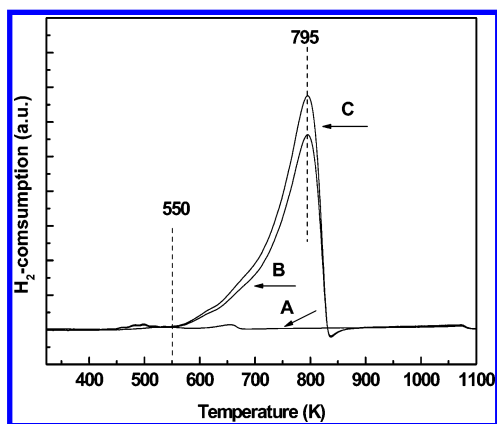


Figure 8. TPR profiles of pure bulk MnO_x: (A) MnO, (B) Mn₃O₄, (C) Mn₂O₃.

might be additional another evidence to support the conclusions from LRS; that is, Mn₂O₃ and Mn₃O₄ nanocrystals are indeed produced on SBA-15. Furthermore, for comparison, data from XPS spectra taken from all reacted catalysts are also presented in Table 2. The stable values of Mn 3s ΔE (eV) suggest that the Mn chemical states are little affected during the subsequent catalytic reaction.

TPR. The TPR profiles in Figure 8 show that H₂ uptake for bulk Mn₃O₄ and Mn₂O₃ starts at ca. 550 K. A sole peak centered at ca. 795 K was observed for both samples, representing the reduction process Mn₂O₃/Mn₃O₄ → MnO,⁴¹ as MnO is irreducible throughout the temperature range. The TPR profiles obtained from the MnO_x nanoparticles (Figure 9) show that the onset of the reduction process for both samples is 440 K and a main reduction peak appears at 617 K, followed by a small one at 740 K for Mn₂O₃/SBA-15, with similar peaks at 620 and 768 K observed for Mn₃O₄/SBA-15. The significant downward shift of the main reduction peak for the MnO_x nanoparticles is possible because of the easy reduction of the small particles. In addition, the small peaks at high temperatures might be caused by the large-sized particles, which are assumed to exist on the external pores of SBA-15.

Catalytic Reactivity. The catalytic properties of these catalysts were tested for the CO oxidation under steady-state conditions in the temperature range of 323–523 K. Results of CO oxidation at a space velocity of 6000 h⁻¹ for various MnO_x samples on SBA catalysts are shown in Figure 10. The light-off (defined as 10% conversion of CO) temperature was measured as 400 K for Mn₃O₄/SBA-15, 425 K for Mn₂O₃/SBA-15, and 450 K for MnO_x/SBA-15 [from Mn(NO₃)₂]. At 500 K,

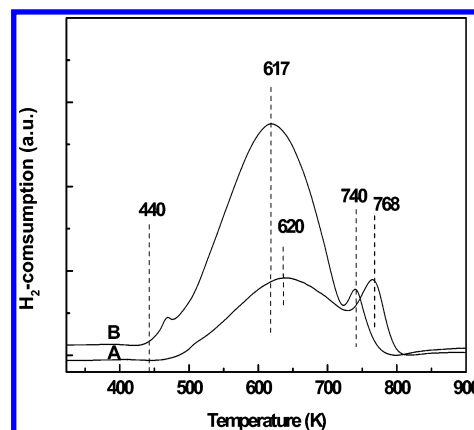


Figure 9. TPR profiles of MnO_x nanocrystals: (A) Mn₃O₄/SBA-15, (B) Mn₂O₃/SBA-15.

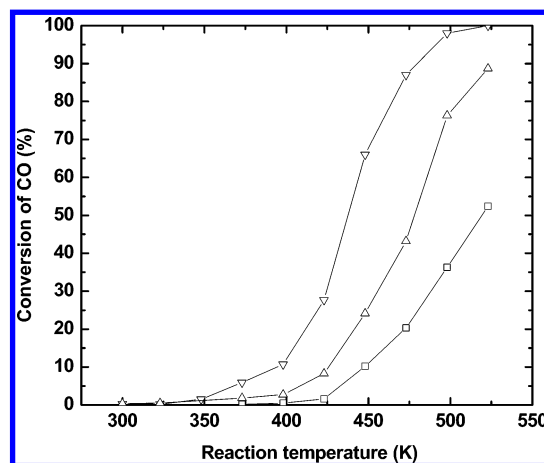


Figure 10. Temperature screening of CO oxidation on supported MnO_x/SBA-15 catalysts: (▽) Mn₃O₄/SBA-15, (Δ) Mn₂O₃/SBA-15, (□) MnO_x/SBA-15 [from Mn(NO₃)₂]. Feed gas = CO (5.0 kPa) + O₂ (5.0 kPa), Ar balance; space velocity = 6000 h⁻¹.

the complete conversion of CO was observed for Mn₃O₄/SBA-15 and ca. 90% for Mn₂O₃/SBA-15. In contrast, only 35% conversion was observed for mixed MnO_x at the same temperature. Clearly, the reactivity of MnO_x/SBA-15 prepared from Mn(NO₃)₂ is lower than that of the MnO_x/SBA-15 from manganese acetyl acetonates. The Mn source plays a decisive role in the fabrication of the active phases for MnO_x nanocrystals, which can markedly affect the catalytic activity.

All nanocatalysts exhibited robust stability, with less than 10% loss of reactivity after 10 h reaction at 473 K. The high stability is due to the fact that the surface structure is unaffected during the reaction, which is partially demonstrated by the XPS analysis (see Table 2). From XPS results, the Mn chemical states for both bulk and supported catalysts are little changed during CO oxidation. This is consistent with the results obtained from LRS by comparing the spectra from fresh and spent catalysts (not shown for the sake of brevity). LRS spectra demonstrated the formation of isolated Mn=O on the present MnO_x/SBA-15 surface, and the electrostatic interaction between CO and those isolated species might be responsible for the rise of catalytic activity from the MnO_x nanoparticles. As Xia et al.⁴² pointed out, in addition to the effect of particles size, many factors can determine the reactivity of manganese oxide nanoparticles, such as the Mn oxidation state, the type and concentration of the loading cations, the local environments of these cations in the catalyst, etc. Relevant studies of the variation in structure of MnO_x from bulk to nanoparticles and its relationship to catalytic

activity are still ongoing in our group. The thermolysis of supported polynuclear metal complexes, in particular, acetyl acetonates, causes reaction with surface hydroxyl groups of the support, and upon thermal treatment, a uniform highly dispersed metal oxide layers can be prepared.^{43–45} This study provided another application of this method: the synthesis of single-crystalline MnO_x on SBA-15.

In summary, the controlled synthesis of MnO_x on SBA-15 can be achieved by molecularly deposited dispersion method, and these materials were found to be catalytically active phases. This study provides a good basis for the development of a new generation of low-temperature combustion catalysts considering their inherently low cost that can potentially be applied in automotive emission control (cool start), air purification, and other pollution control processes.

4. Conclusions

The important conclusions derived from the present study can be summarized as follows:

(i) Thermolysis of Mn acetylacetonates inside mesoporous SBA-15 was found to be an effective method for the synthesis of Mn₃O₄ and Mn₂O₃ nanocrystals.

(ii) The framework of SBA-15 is unaffected during the fabrication of MnO_x nanoparticles (XRD and TEM). Most of the nanoparticles were found to be confined inside the pores of SBA-15 (N₂ adsorption–desorption, TEM). Nanoparticles with the hausmannite Mn₃O₄ and bixbyite α -Mn₂O₃ structures were identified (XRD).

(iii) The surface structures of the MnO_x nanocrystals were determined using XPS and LRS. The LRS results show that the surface structures of the as-prepared MnO_x nanoparticles are similar to those of their bulk counterparts. Vibrations at 940 cm⁻¹ for Mn₃O₄/SBA-15 and 974 cm⁻¹ for Mn₂O₃/SBA-15 are attributed to the terminal Mn=O bonds, which is obscured for bulk MnO_x. The surface structure of MnO_x nanoparticles is very stable during CO oxidation, as indicated by the unchanged Mn valence and Mn/O atomic ratio analyzed by XPS.

(iv) The MnO_x nanoparticles prepared from manganese acetyl acetonates exhibited high catalytic reactivity compared to those prepared from Mn(NO₃)₂.

References and Notes

- Chabre, Y.; Pannetier, J. *Prog. Solid State Chem.* **1995**, *23*, 1.
- Whittingham, M. S.; Zavalig P. Y. *Solid State Ionics* **2003**, *131*, 109.
- Shen, Y. F.; Zerger, P. R.; DeGuzman, N. R.; Suib, L. S.; McCurdy, L.; Potter, I. D.; O'Young, C. L. *Science* **1993**, *260*, 511.
- Yin, M.; O'Brien S. J. *Am. Soc. Chem.* **2003**, *125*, 10180.
- Brock, S. L.; Duan, N.; Tian, Z. R.; Giraldo, O.; Zhou, H.; Suib, S. L. *Chem. Mater.* **1998**, *10*, 2619.
- Fernandez-Garcia, M.; Martinez-Arias, A.; Hanson, J. C.; Rodriguez, J. A. *Chem. Rev.* **2004**, *104*, 4063.
- Xiong, Y.; Xie, Y.; Li, Z.; Wu, C. *Chem.—Eur. J.* **2003**, *9*, 1645.
- Tian, B.; Liu, X.; Yang, H.; Xie, S.; Yu, C.; Tu, B.; Zhao, D. Y. *Adv. Mater.* **2003**, *15*, 1370.
- Escay, V.; Imperor-Clerc, M.; Bazin, D.; Davidson, A. C. *R. Chim.* **2005**, *8*, 663.
- Kanungo, S. J. *Catal.* **1979**, *58*, 419.
- Strohmeier B. R.; Hercules, D. M. *J. Phys. Chem.* **1984**, *88*, 4922.
- Folch B.; Larionova J.; Guari Y.; Guerin C.; Mehdi A.; Reye C. J. *Mater. Chem.* **2004**, *14*, 2730.
- Imperor-Clerc, M.; Bazin, D.; Appay M.-D.; Beaunier P.; Davidson, A. *Chem. Mater.* **2004**, *16*, 1813.
- Mita, Y.; Sakai, Y.; Izaki, D.; Kobayashi, M.; Endo, S.; Mochizui, S. *Phys. Status Solidi* **2001**, *223*, 247.
- Huang, M. H.; Mao, S.; Feick, H.; Yan, H.; Wu, Y.; Kind, H.; Weber, E.; Russo, R.; Yang, P. *Science* **2001**, *292*, 1897.
- Han Y.-F.; Zhong Z.-Y.; Chen L.-W.; Widjaja, E.; Chen F.; Liu Y.; Wang, Z. Mechanism Study for CO Oxidation over Manganese Oxides Catalysts. Presented at Singapore International Chemical Conference 4, Singapore, Dec 8–10, 2005.
- Zhao, D. Y.; Huo, Q. S.; Feng, J. L.; Chmelka, B. E.; Stucky, G. D. *J. Am. Soc. Chem.* **1998**, *120*, 6024.
- Zhao, D. Y.; Feng, J. L.; Huo, Q. S.; Melosh, N.; Fredrickson, G. H.; Chmelka, B. F.; Stucky, G. D. *Science* **1998**, *279*, 548.
- Yang, H.; Shi, Q.; Tian, B.; Lu, Q.; Gao, F.; Xie, S.; Fan, J.; Yu, C.; Tu, B.; Zhao, D. Y. *J. Am. Soc. Chem.* **2003**, *125*, 4724.
- Einaga, H.; Futamura, S. *J. Catal.* **2004**, *227*, 304.
- Döbber, D.; Kiessling, D.; Schmitz, W.; Wendt, G. *Appl. Catal. B: Environ.* **2004**, *52*, 135.
- Han, Y.-F.; Kahlich, M.; Kinne, M.; Behm, R. J. *Appl. Catal. B: Environ.* **2004**, *50*, 209.
- Han, Y.-F.; Kahlich, M.; Kinne, M.; Behm, R. J. *Appl. Catal. B: Environ.* **2004**, *52*, 123.
- Han, Y.-F.; Wang, J.-H.; Kumar, D.; Goodman, D. W. *J. Catal.* **2005**, *232*, 467.
- Scofield, J. H. *J. Electron Spectrosc. Relat. Phenom.* **1976**, *8*, 129.
- Moulder, J. F.; Stickle, W. F.; Sobol, P. E.; Bomben, K. D. *Handbook of X-ray Photoelectron Spectroscopy*; Chastain, J., King, C., Jr., Eds.; Physical Electronics, Inc.: Eden Prairie, MN, 1995.
- Lee S.-J.; Gavrilidis A.; Pankhurst Q. A.; Kyek A.; Wagner F. E.; Wong P. C. L.; Yeung K. L. *J. Catal.* **2001**, *200*, 298.
- Chua, Y. T.; Stair, P. C.; Wachs, I. E. *J. Phys. Chem. B* **2001**, *105*, 8600.
- Bernard, M.-C.; Goff, A. H.; Thi, B. V.; De Torresi, S. C. *J. Electrochem. Soc.* **1993**, *140*, 3065.
- Handbook of Vibrational Spectroscopy*; Chalmers, J. M., Griffiths, P. R., Eds.; John Wiley & Sons Ltd.: West Sussex, U.K., 2002.
- Buciuman F.; Patcas F.; Cracium R.; Zahn, D. R. T. *Phys. Chem. Chem. Phys.* **1999**, *1*, 185.
- Zuo J.; Xu C.; Liu Y.; Qian Y. *Nanostruct. Mater.* **1998**, *10*, 1331.
- Ludvigsson M.; Lindgren J.; Tegenfeldt J. *J. Mater. Chem.* **2001**, *11*, 1269.
- Morey M.; Davidson A.; Stucky G. *Microporous Mater.* **1996**, *6*, 99.
- Zhao, L. Z.; Young, V. J. *Electron Spectrosc. Relat. Phenom.* **1984**, *34*, 45.
- Elp, J. van; Potze R. H.; Eskes, H.; Berger, R.; Sawatzky, G. A. *Phys. Rev. B* **1991**, *44*, 1530.
- Castro, V. D.; Polzonetti, G. J. *Electron Spectrosc. Relat. Phenom.* **1989**, *48*, 117.
- Gardner, S. D.; Hoflund, G. R.; Davidson, M. R. *Langmuir* **1991**, *7*, 2140.
- Grzybek, T.; Klinik, J.; Rogoz, M.; Papp, H. J. *Chem. Soc., Faraday Trans.* **1998**, *94*, 2843.
- Kapteijn, F.; Langeveld, D. van; Moulijn, J. A.; Andreini, A. J. *Catal.* **1994**, *150*, 94.
- de la Pena O'Shea V. A.; Alvarez-Galvan M. C.; Fierro, J. L. G.; Arias, P. L. *Appl. Catal. B: Environ* **2004**, *57*, 191.
- Xia, G. G.; Yin, Y. G.; Willis, W. S.; Wang, J. Y.; Suib, S. L. *J. Catal.* **1999**, *185*, 91.
- White, M. G. *Catal. Today* **1993**, *18*, 73.
- Baltes, M.; van Der voort, C. P.; Weckhuysen, B. M.; Schoonheydt, R. A.; Vansant, E. F. *J. Catal.* **2001**, *197*, 160.
- van Der voort, C. P.; Possemiers, K.; Vansant, E. F. *J. Chem. Soc., Faraday Trans.* **1996**, *92*, 843.